Article

A planetary collision afterglow and transit of the resultant debris cloud

https://doi.org/10.1038/s41586-023-06573-9

Received: 5 May 2023

Accepted: 25 August 2023

Published online: 11 October 2023

Check for updates

Matthew Kenworthy[1,21]✉, Simon Lock[2,21], Grant Kennedy[3,4,21], Richelle van Capelleveen[1,21], Eric Mamajek[5,6,21], Ludmila Carone[7,21], Franz-Josef Hambsch[8,9,10], Joseph Masiero[11], Amy Mainzer[12], J. Davy Kirkpatrick[11], Edward Gomez[13,14], Zoë Leinhardt[15], Jingyao Dou[15], Pavan Tanna[16], Arttu Sainio[17], Hamish Barker[18], Stéphane Charbonnel[19], Olivier Garde[19], Pascal Le Dû[19], Lionel Mulato[19], Thomas Petit[19] & Michael Rizzo Smith[20]

Planets grow in rotating disks of dust and gas around forming stars, some of which can subsequently collide in giant impacts after the gas component is removed from the disk[1–3]. Monitoring programmes with the warm Spitzer mission have recorded substantial and rapid changes in mid-infrared output for several stars, interpreted as variations in the surface area of warm, dusty material ejected by planetary-scale collisions and heated by the central star: for example, NGC 2354–ID8 (refs. 4,5), HD 166191 (ref. 6) and V488 Persei[7]. Here we report combined observations of the young (about 300 million years old), solar-like star ASASSN-21qj: an infrared brightening consistent with a blackbody temperature of 1,000 Kelvin and a luminosity that is 4 percent that of the star lasting for about 1,000 days, partially overlapping in time with a complex and deep, wavelength-dependent optical eclipse that lasted for about 500 days. The optical eclipse started 2.5 years after the infrared brightening, implying an orbital period of at least that duration. These observations are consistent with a collision between two exoplanets of several to tens of Earth masses at 2–16 astronomical units from the central star. Such an impact produces a hot, highly extended post-impact remnant with sufficient luminosity to explain the infrared observations. Transit of the impact debris, sheared by orbital motion into a long cloud, causes the subsequent complex eclipse of the host star.

The otherwise unexceptional star 2MASS J08152329-3859234 underwent a sudden optical-dimming event in December 2021[8,9] and was assigned the identifier ASASSN-21qj by the All Sky Automated Survey for Supernovae (ASAS-SN)[10,11]. Here we combine both optical (from the Las Cumbres Observatory Global Telescope Network (LCOGT)) and infrared (from the Wide-field Infrared Survey Explorer (WISE) satellite) observations of ASASSN-21qj for the years before and after this dimming event (Fig. 1). Optical multiband photometry shows a wavelength-dependent depth consistent with extinction by submicrometre particles. About 900 days before the optical-dimming event, the ASASSN-21qj system showed a notable brightening in the infrared, of 0.4 magnitudes at 3.8 μm (W1) and 0.8 magnitudes at 4.5 μm (W2). Before this time, the infrared brightness was consistent with being purely stellar. The increased infrared fluxes indicate that, as well as the quiescent stellar flux, there was new emission at a temperature of approximately 1,000 K. Such a notable combination of observations, particularly the 2.5-year delay between the infrared and optical variation, requires an explanation.

The optical and infrared light curves (Fig. 1) provide key constraints on any proposed scenario. The post-brightening infrared fluxes in the W1 and W2 WISE passbands are consistent with emission at a blackbody temperature of 1,000 ± 100 K and this temperature is sustained, within error, for the remainder of our observation window, despite a decline in the total flux. For an emitter located at the distance of ASASSN-21qj from Earth, and the observed maximum luminosity of approximately 0.04 $L_\star$, this implies an emitting area of 0.01 AU^2, equivalent to an object with a radius of 7 $R_\odot$, or 750 $R_{\rm Earth}$. If this emission was from material—such as dust—passively heated by proximity to the star, then that material must have been generated and remained within about 0.1 AU to produce the observed temperature.

One possible explanation is that we are observing two unrelated but coincidental phenomena: a warm-dust-generating collision within

[1]Leiden Observatory, Leiden University, Leiden, The Netherlands. [2]School of Earth Sciences, University of Bristol, Bristol, UK. [3]Department of Physics, University of Warwick, Coventry, UK. [4]Centre for Exoplanets and Habitability, University of Warwick, Coventry, UK. [5]Jet Propulsion Laboratory, California Institute of Technology, Pasadena, CA, USA. [6]Department of Physics and Astronomy, University of Rochester, Rochester, NY, USA. [7]Space Research Institute, Austrian Academy of Sciences, Graz, Austria. [8]Vereniging Voor Sterrenkunde, Brugge, Belgium. [9]American Association of Variable Star Observers, Cambridge, MA, USA. [10]Bundesdeutsche Arbeitsgemeinschaft für Veränderliche Sterne e.V., Berlin, Germany. [11]IPAC, California Institute of Technology, Pasadena, CA, USA. [12]Lunar and Planetary Laboratory, University of Arizona, Tucson, AZ, USA. [13]Las Cumbres Observatory, Goleta, CA, USA. [14]School of Physics and Astronomy, Cardiff University, Cardiff, UK. [15]School of Physics, HH Wills Physics Laboratory, University of Bristol, Bristol, UK. [16]Institute of Astronomy, University of Cambridge, Cambridge, UK. [17]Independent researcher, Järvenpää, Finland. [18]Variable Stars South, Nelson, New Zealand. [19]Southern Spectroscopic Project Observatory Team, Chabons, France. [20]Department of Astronomy, The Ohio State University, Columbus, OH, USA. [21]These authors contributed equally: Matthew Kenworthy, Simon Lock, Grant Kennedy, Richelle van Capelleveen, Eric Mamajek, Ludmila Carone. ✉e-mail: kenworthy@strw.leidenuniv.nl

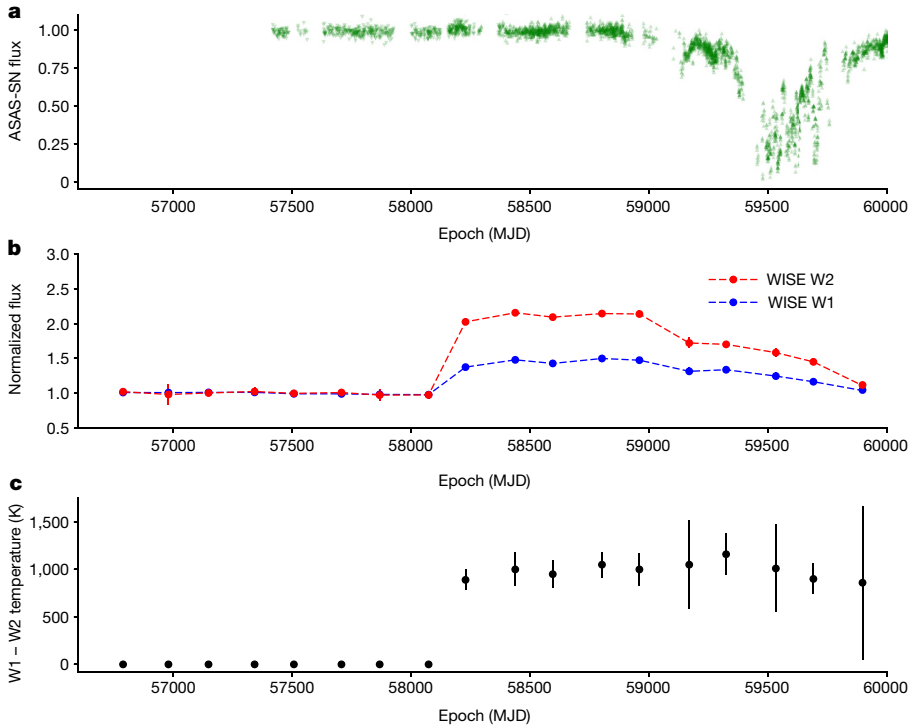

Fig. 1 | Optical and infrared photometry of ASASSN-21qj. a, Normalized optical photometry from ASAS-SN in the V-band and the g′-band. **b**, Fractional flux increase in brightness of ASASSN-21qj in both the W1 and W2 bands, for which a value of 1.0 represents the stellar contribution alone. **c**, Calculated NEOWISE colour temperature estimated from the photometry of the two bands. The colour temperature is plotted as zero when there is no infrared excess and is consistent with a temperature of 1,000 K while the excess is present. Error bars are shown at 1σ confidence.

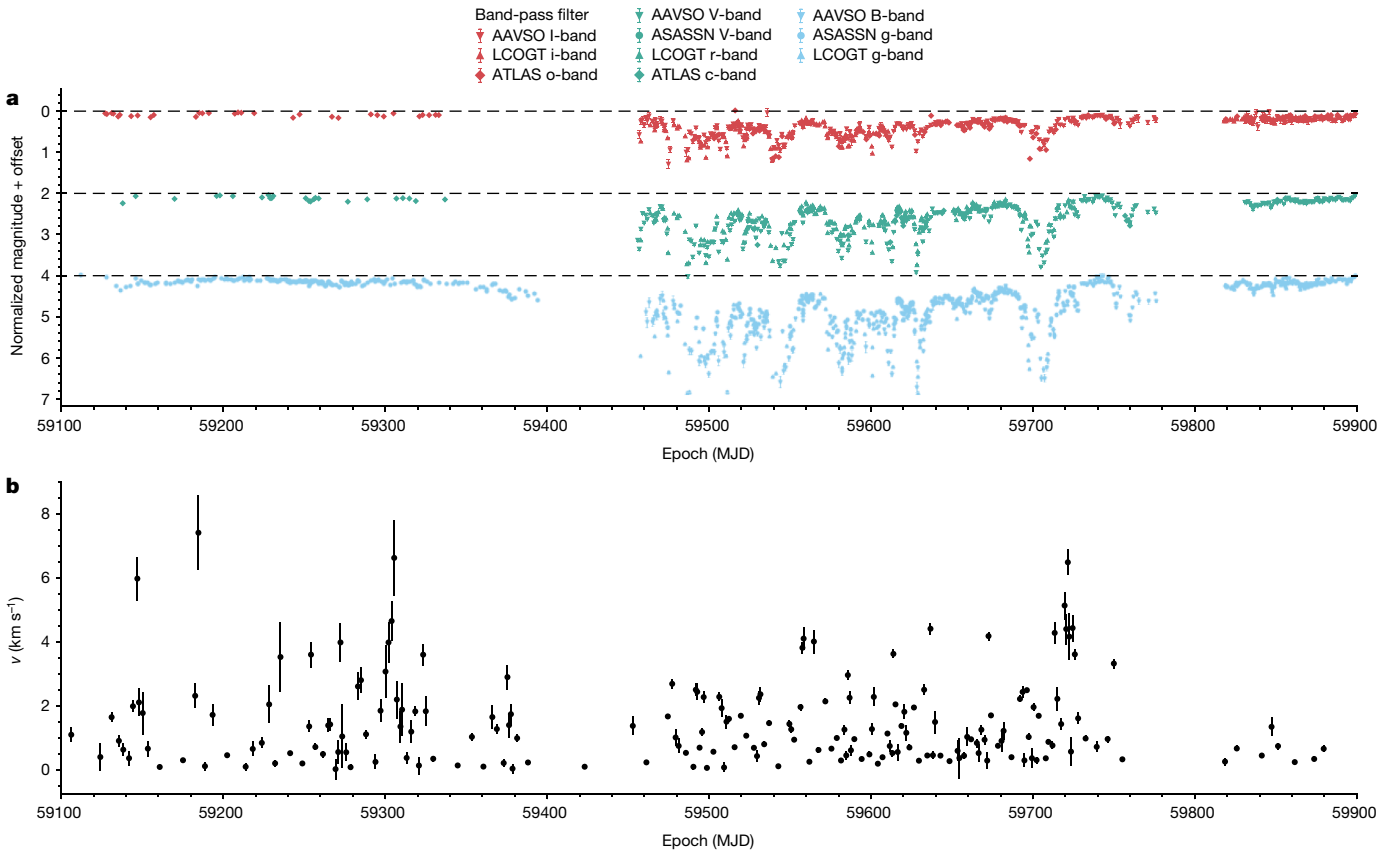

Fig. 2 | The light curve of ASASSN-21qj from several different photometric surveys and the derived transverse velocities. a, The eclipse depth is deeper for shorter wavelengths, indicating that the transiting material is dominated by submicrometre-sized grains. **b**, Transverse velocities derived from the light-curve gradients. These are lower limits to the true velocity and thus imply that the transiting material is closer to the star than 16 AU. Error bars are shown at 1σ confidence.

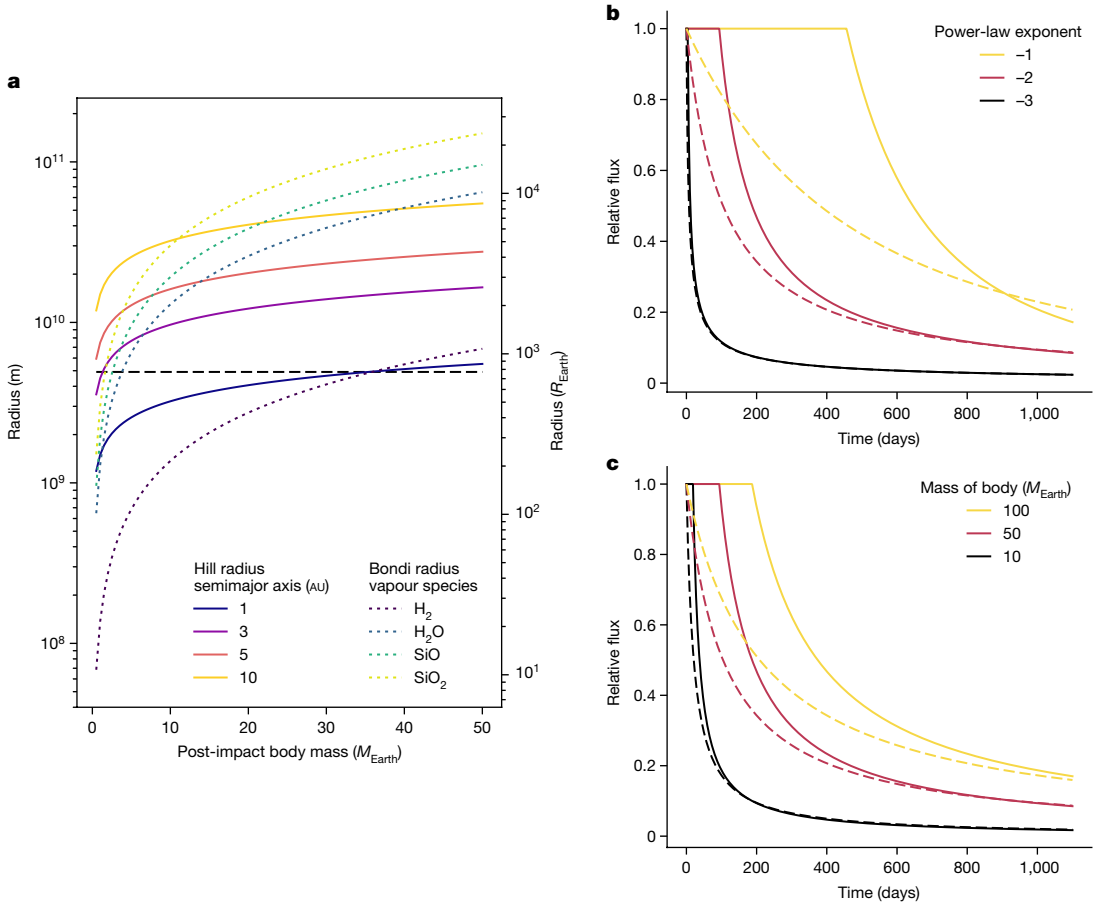

Fig. 3 | The size and temporal evolution of a post-impact body. A post-impact body of a few to tens of Earth masses could be large enough to explain the observed increase in thermal emission from ASASSN-21qj and the subsequent infrared fluxes. **a**, The Hill radii for bodies at different semimajor axes (solid coloured lines) and the Bondi radii (dashed lines) assuming different compositions for the vapour of the post-impact body. The horizontal black dashed line shows the radius required to explain the observed flux at the inferred emission temperature of 1,000 K. **b**,**c**, The change in excess flux owing to a post-impact body with time for a simple model of cooling of a post-impact body for different power-law surface density profiles (**b**; equation (1)) and for different mass bodies (**c**). Each example had an initial radius of 7 $R_{\odot}$, a radiative temperature of 1,000 K and a corresponding initial flux of 0.04 $L_{\star}$, as estimated for the observed infrared emitter. The solid lines are profiles that can have non-zero initial density at the initial emitting radius and the dashed lines are for ones that are forced to have zero density at the initial emitting radius. When not stated, the mass of the post-impact body was 50 M_{Earth}, the power-law exponent is −2 and the size of the central region was 10 R_{Earth}.

0.1 AU of the star, with a separate object transiting the star 900 days later. Two events that are themselves very rare occurring independently in one system is, however, highly improbable. A second explanation is that warm dust is generated close to the star and causes the optical transit, but this requires a fine-tuned configuration in which the star is optically blocked by scale-height variations in the resulting disk.

Instead, we suggest that we are observing the aftermath of a single collision between super-Earths or mini-Neptunes—a so-called giant impact—between 2 and 16 AU from the star. These distances are determined, respectively, by the delay between the infrared brightening and the optical eclipse (Fig. 1) and by gradients in the optical light curve (Fig. 2). In contrast to other extreme-debris-disk events in which the star heats the dust, we propose that the infrared emission is directly from the post-impact body[12,13] and that impact debris produced the optical transit. Giant impacts are a common occurrence in planet formation[14,15] and also occur during instabilities in older systems[16]; this would explain the observations with a single event of a type that is expected for systems with ages such as that of ASASSN-21qj.

Giant impacts are one of the most energetic events that planets experience. For example, the kinetic energy of impacts between two half-Neptune-mass bodies range from 10^{33} to 10^{34} J, enough to vaporize the colliding bodies several times over. A large fraction of this energy is dissipated in the colliding bodies and post-impact bodies are substantially melted and vaporized[12,17,18]. Furthermore, extreme torques exerted in impacts often produce rapidly rotating bodies[12]. Such low-density and rotationally flattened bodies can be hundreds of times larger than the pre-impact planets[12], with correspondingly large radiative surfaces.

Giant impacts produce substantial amounts of debris, typically around 1% of the colliding mass, that is injected into orbit around the host star[19,20]. Impact ejecta have a wide range of sizes, from submicrometre dust to planetesimals of tens to hundreds of kilometres across, and often contain the most highly heated material[21–23]. For sufficiently high impact velocities (>1 km s^{-1} for water ice and >8 km s^{-1} for forsterite), a substantial fraction of this material is vaporized[23–25]. Shearing of droplets and cooling and condensation of vapour produces a population of small dust grains and solid spherules. The size distribution of this fraction of the debris is uncertain, owing to difficulties in modelling condensate nucleation and break-up, but previous work suggests that debris could range in size from submicrometre to decimetres[21,26]. The wavelength-dependent eclipse suggests that the optical depth of the transiting dust cloud is dominated by submicrometre grains,

consistent with these previous estimates. Although the fading of the excess infrared flux occurs within 100 days of the start of the optical transit, we consider the timing to be coincidental because there is no clear correspondence between the light curves, for example, no change in the (6-month cadence) infrared flux when the star dims in the optical wavelengths just before MJD 59500.

The radiative flux from post-impact bodies has not been explored in depth. Computational-resource limitations make resolving the low-density outer regions and photosphere of post-impact bodies extremely challenging. However, preliminary simulations of impacts between super-Earth and mini-Neptunes place an approximate lower limit on the extent of post-impact bodies and show that post-impact bodies can extend to hundreds of Earth radii. Such an object radiating at about 1,000 K would produce a flux comparable with the 0.04 $L_\star$ inferred from our observations.

Independent of impact simulations, there are fundamental limits on the size of post-impact bodies from the Hill and Bondi radii. Any post-impact structure must lie within the Hill sphere, the distance within which the gravity of an object dominates over that of the star. Furthermore, only vapour within the Bondi radius would be bound to the post-impact body. Figure 3a shows the Hill radii at different distances from ASASSN-21qj (solid lines) and the Bondi radii for example gas species (dashed lines). Beyond 2.4 AU, the Hill radii of greater-than-Earth-mass bodies are large enough to accommodate a post-impact body capable of producing the required infrared flux (approximately 7 $R_\star$, dashed line). Heavier gases (H_2O, SiO and SiO_2) are also bound to bodies of more than a few Earth masses. A post-impact body of a few Earth masses can hence theoretically produce the observed infrared emission, with a photosphere that is dust and/or vapour.

A key line of evidence for direct detection of a post-impact body is the constant emission temperature. It is argued[20] that rocky post-impact bodies become optically thin at low pressures at which radiative loss drives rapid condensation of the rock vapour. The emission temperature is then set by the liquid–vapour phase boundary and is constant until the post-impact body almost fully condenses[20,27]. The dew point (onset of condensation) and bubble point (onset of substantial vaporization) of material with bulk silicate Earth composition are similar (about 2,300 K, within roughly 100 K (refs. 20,28)) at the low pressures of the photosphere of a post-impact body. However, even small amounts of water (10^{-3} mole fraction) may lower the bubble and dew points for silicates by approximately 100 K (refs. 20,28). The emission temperature of bodies produced by collisions of protoplanets composed of rock and ices/volatiles could be buffered at about 1,000 K during early evolution.

The temporal variation of flux from a post-impact body is controlled by evolution of the sizes of the bodies, which is governed by several competing factors[20,29], including radiative energy loss, viscous spreading and mass and angular momentum transfer by condensates. For silicate-dominated post-impact bodies, the high emission temperature means that radiative cooling dominates and the post-impact body contracts rapidly, fully condensing over years to thousands of years[20,29]. The body we observed has a much lower emission temperature and contracted much more slowly. Figure 3b,c shows the evolution of conceptual post-impact bodies in the limiting case that radiative cooling dominates. If sufficient mass is injected into the outer regions (that is, less negative power-law exponents), the observed flux can remain constant for an initial period and then decays over the order of hundreds of days, in agreement with infrared observations. Further work is required to understand the structure and evolution of bodies produced by impacts between super-Earths and mini-Neptunes of different compositions and identify temporal-flux variations consistent with our observations.

Online content

Any methods, additional references, Nature Portfolio reporting summaries, source data, extended data, supplementary information, acknowledgements, peer review information; details of author contributions and competing interests; and statements of data and code availability are available at https://doi.org/10.1038/s41586-023-06573-9.

1. Williams, J. P. & Cieza, L. A. Protoplanetary disks and their evolution. *Annu. Rev. Astron. Astrophys.* **49**, 67–117 (2011).
2. Wyatt, M. C., Panić, O., Kennedy, G. M. & Matrà, L. Five steps in the evolution from protoplanetary to debris disk. *Astrophys. Space Sci.* **357**, 103 (2015).
3. Hughes, A. M., Duchêne, G. & Matthews, B. C. Debris disks: structure, composition, and variability. *Annu. Rev. Astron. Astrophys.* **56**, 541–591 (2018).
4. Meng, H. Y. A. et al. Large impacts around a solar-analog star in the era of terrestrial planet formation. *Science* **345**, 1032–1035 (2014).
5. Su, K. Y. L. et al. Extreme debris disk variability: exploring the diverse outcomes of large asteroid impacts during the era of terrestrial planet formation. *Astron. J.* **157**, 202 (2019).
6. Su, K. Y. L., Kennedy, G. M., Schlawin, E., Jackson, A. P. & Rieke, G. H. A star-sized impact-produced dust clump in the terrestrial zone of the HD 166191 system. *Astrophys. J.* **927**, 135 (2022).
7. Rieke, G. H., Su, K. Y. L., Melis, C. & Gáspár, A. Extreme variability of the V488 Persei debris disk. *Astrophys. J.* **918**, 71 (2021).
8. Rizzo Smith, M. et al. ASASSN-21qj: a rapidly fading, Sun-like star. *The Astronomer's Telegram* 14879 (2021).
9. Rizzo Smith, M. et al. An update on ASASSN-21qj: a rapidly fading, Sun-like star; back with a vengeance. *The Astronomer's Telegram* 15531 (2022).
10. Shappee, B. J. et al. The man behind the curtain: X-rays drive the UV through NIR variability in the 2013 active galactic nucleus outburst in NGC 2617. *Astrophys. J.* **788**, 48 (2014).
11. Kochanek, C. S. et al. The All-Sky Automated Survey for Supernovae (ASAS-SN) light curve server v1.0. *Publ. Astron. Soc. Pac.* **129**, 104502 (2017).
12. Lock, S. J. & Stewart, S. T. The structure of terrestrial bodies: impact heating, corotation limits, and synestias. *J. Geophys. Res. Planets* **122**, 950–982 (2017).
13. Miller-Ricci, E., Meyer, M. R., Seager, S. & Elkins-Tanton, L. On the emergent spectra of hot protoplanet collision afterglows. *Astrophys. J.* **704**, 770–780 (2009).
14. Schlichting, H. E. in *Handbook of Exoplanets* (eds Deeg, H. J. & Belmonte, J. A.) 2345–2364 (Springer, 2018).
15. D'Angelo, G. & Lissauer, J. J. in *Handbook of Exoplanets* (eds Deeg, H. J. & Belmonte, J. A.) 2319–2343 (Springer, 2018).
16. Kaib, N. A. & Chambers, J. E. The fragility of the terrestrial planets during a giant-planet instability. *Mon. Not. R. Astron. Soc.* **455**, 3561–3569 (2016).
17. Nakajima, M. & Stevenson, D. J. Melting and mixing states of the Earth's mantle after the Moon-forming impact. *Earth Planet. Sci. Lett.* **427**, 286–295 (2015).
18. Carter, P. J., Loc, S. J. & Stewart, S. T. The energy budgets of giant impacts. *J. Geophys. Res. Planets* **125**, e2019JE006042 (2020).
19. Canup, R. M. & Asphaug, E. Origin of the Moon in a giant impact near the end of the Earth's formation. *Nature* **412**, 708–712 (2001).
20. Lock, S. J. et al. The origin of the Moon within a terrestrial synestia. *J. Geophys. Res. Planets* **123**, 910–951 (2018).
21. Benz, W., Anic, A., Horner, J. & Whitby, J. A. in *Mercury* (eds Balogh, A. et al.) 7–20 (Springer, 2008).
22. Leinhardt, Z. M., Dobinson, J., Carter, P. J. & Lines, S. Numerically predicted indirect signatures of terrestrial planet formation. *Astrophys. J.* **806**, 23 (2015).
23. Carter, P. J. & Stewart, S. T. Colliding in the shadows of giants: planetesimal collisions during the growth and migration of gas giants. *Planet. Sci. J.* **1**, 45 (2020).
24. Stewart, S. T., Seifter, A. & Obst, A. W. Shocked H_2O ice: thermal emission measurements and the criteria for phase changes during impact events. *Geophys. Res. Lett.* **35**, L23203 (2008).
25. Davies, E. J. et al. Silicate melting and vaporization during rocky planet formation. *J. Geophys. Res. Planets* **125**, e2019JE006227 (2020).
26. Johnson, B. C., Minton, D. A., Melosh, H. J. & Zuber, M. T. Impact jetting as the origin of chondrules. *Nature* **517**, 339–341 (2015).
27. Caracas, R. & Stewart, S. T. No magma ocean surface after giant impacts between rocky planets. *Earth Planet. Sci. Lett.* **608**, 118014 (2023).
28. Fegley, B.Jr, Lodders, K. & Jacobson, N. S. Chemical equilibrium calculations for bulk silicate earth material at high temperatures. *Geochemistry* **83**, 125961 (2023).
29. Lock, S. J., Stewart, S. T. & Ćuk, M. The energy budget and figure of Earth during recovery from the Moon-forming giant impact. *Earth Planet. Sci. Lett.* **530**, 115885 (2020).

Publisher's note Springer Nature remains neutral with regard to jurisdictional claims in published maps and institutional affiliations.

Springer Nature or its licensor (e.g. a society or other partner) holds exclusive rights to this article under a publishing agreement with the author(s) or other rightsholder(s); author self-archiving of the accepted manuscript version of this article is solely governed by the terms of such publishing agreement and applicable law.

© The Author(s), under exclusive licence to Springer Nature Limited 2023

Methods

The stellar properties of ASASSN-21qj (Gaia DR3 5539970601632026752 = 2MASS J08152329-3859234) are listed in Extended Data Table 1, showing that ASASSN-21qj is consistent with being a G2-type dwarf star. Where necessary, we assume a stellar mass equal to the Sun. ASASSN-21qj has a neighbour (Gaia DR3 5539970597334497024 = 2MASS J08152298-3859244), which is a visual double. On the basis of the Gaia DR3 mean International Celestial Reference System (ICRS) position for epoch 2016.0, the visual companion lies at a separation ρ = 3,738.243 ± 0.062 mas and at position angle θ = 249.977°. Their parallaxes (ϖ = 1.7631 ± 0.0112 mas versus 1.4711 ± 0.0523 mas) differ by 5.5σ and proper motions (μ_α = −9.692 ± 0.012, μ_δ = 7.349 ± 0.012 mas year^{-1} versus μ_α = −0.114 ± 0.055, μ_δ = 6.419 ± 0.053 mas year^{-1}) differ by a factor of 2. The large differences in distance and proper motions suggest that these stars are not associated.

The stellar photospheric flux was estimated by fitting stellar models to GAIA, APASS and DENIS and WISE optical/near-infrared photometry (the 2MASS J photometry is an upper limit and H and K_s are flagged as contaminated). Extended Data Fig. 1 shows the resulting models (the dashed line is discussed below). The ALLWISE photometry (around 2010) is consistent with the Near-Earth Object Wide-field Infrared Survey Explorer (NEOWISE) photometry pre-brightening nearly 10 years later.

A fit using the method in ref. 30 with GAIA and DENIS photometry finds that the WISE W1/2 fluxes are about 20% too high, but better agreement is found with APASS photometry. The difference is explained by the fact that WISE and APASS have lower spatial resolution and include the flux of the approximately 2 mag fainter visual double to the west of ASASSN-21qj (which is visible in 2MASS). The best-fit stellar effective temperature is 5,560 ± 100 K. We do not find that reddening is needed for these models; although there is relatively little photometry with which to strongly constrain both $T_{\rm eff}$ and A_V, the $T_{\rm eff}$ from GAIA DR3 is 5,760 ± 10 K, which suggests that the conclusion of little reddening is valid. Primarily, we conclude that there is no indication that ASASSN-21qj showed evidence for an infrared excess before the brightening seen by NEOWISE.

To estimate the infrared excess properties, we fit the same models but now including the first five post-brightening NEOWISE data points. We correct for the nearby source by using the GAIA photometry or the star and the post-brightening/pre-brightening difference for the WISE excess flux. This fit yields the fractional luminosity $L_{\rm dust}/L_\star$ = 0.04 ± 0.005 and a dust temperature 950 ± 30 K. To estimate the dust temperature as a function of time, we simply subtract the median pre-brightening W1/2 fluxes, with the r.m.s. of these values as the uncertainty (see Fig. 1). The temperature uncertainty increases as the excess fades; the excess flux uncertainty depends on both the observed flux and the stellar flux, and as the excess decreases, the stellar uncertainty (which is constant) becomes an increasingly large fraction of the excess. These fluxes therefore exclude the contaminating flux from the nearby object and are consistent with the spectral energy distribution (SED)-derived dust temperature.

Converting dust temperatures to stellocentric radii is uncertain because dust temperature depends on grain size. Typically, the radius derived under the assumption of blackbody emission is an underestimate by a factor of up to five[31,32]. Thus, we conclude that the dust location might, in the most extreme case, be as far as 1 AU, but not sufficiently far to explain the 900-day delay between the WISE and optical-flux variations, which requires a distance of at least 2 AU.

Observations

The beginning of the eclipse was announced[8] by the ASAS-SN survey, which prompted several observing campaigns at optical wavelengths and an ALMA observation at Band 7 (programme 2019.A.00040.S). The photometric data and passband filters are listed in Extended Data Table 2.

The All Sky Automated Survey (ASAS)[33–35] is a survey consisting of two observing stations, one in Las Campanas, Chile and the other on Maui, Hawaii. Each observatory is equipped with two charge-coupled device (CCD) cameras using V and I filters and commercial f = 200 mm, D = 100 mm lenses, although both larger (D = 250 mm) and smaller (50–72 mm) lenses were used at earlier times. Most of the data are taken with a pixel scale of about 15″. ASAS splits the sky into 709 partially overlapping 9° × 9° fields, taking—on average—150 3-min exposures per night, leading to a variable cadence of 0–2 frames per night. Depending on the equipment used and the mode of operation, the ASAS limiting magnitude varied between 13.5 and 15.5 mag in V and the saturation limit was 5.5 to 7.5 mag. Precision is around 0.01–0.02 mag for bright stars and below 0.3 mag for the fainter ones. ASAS photometry is calibrated against the Tycho Catalogue and its accuracy is limited to 0.05 mag for bright, non-blended stars.

The ASAS-SN[10,11] consists of five stations around the globe, with each station hosting four telescopes with a shared mount. The telescopes consist of a 14-cm aperture telephoto lens with a field of view of approximately 4.5° × 4.5° and an 8.0″ pixel scale. Two of the original stations (one in Hawaii and one in Chile) were initially fitted with V-band filters, but now these and all the other stations (Texas, South Africa and a second station in Chile) observe with g′-band filters down to 18 mag.

The Remote Observatory Atacama Desert (ROAD)[36] is a fully automated telescope located in Chile that obtains nightly photometry in Astrodon B, V and I bands for a wide range of astronomical projects. It consists of a 40-cm f/6.8 Optimized Dall-Kirkham and uses a Finger Lakes Instruments camera with a 4k × 4k array with pixels of 9 µm in size. Data are reduced using a custom pipeline and then published on the AAVSO website.

LCOGT is a network of 25 fully robotically operated telescopes distributed over seven sites located all around the globe. These telescopes are designed to observe transient astronomical events at optical and near-infrared wavelengths. LCOGT provides a large variety of filter options, but the data we collected are in SDSS g′, r′ and i′ bands. All data are automatically processed and calibrated by the BANZAI pipeline. The visual companion caused complications in the automatic aperture extraction routine of BANZAI; sometimes, correct apertures were extracted for both ASASSN-21qj and the nearby star and sometimes both sources were extracted in one large aperture, often with an offset from the true centre of ASASSN-21qj. To correct this, the last two stages of the BANZAI routine, aperture extraction and photometry calibration, were modified for this specific situation. The calibrated magnitudes of all sources in the frames are computed using the default BANZAI photometry calibration routine.

ATLAS is a project that searches for near-Earth asteroids down to a magnitude of 19 (ref. 37). Two filters were obtained, the o (orange) and c (cyan) filters, respectively. The data consist of two to four photometric points observed each night when conditions permitted. Photometry with large errors was rejected in a first pass and then the remaining observations during a night were averaged and an error based on the r.m.s. of these nightly points was calculated. The photometry covers the time period in which the collision event occurred.

The Transiting Exoplanet Survey Satellite (TESS)[38] is a satellite designed to survey for transiting exoplanets among the brightest and nearest stars over most of the sky. The TESS satellite orbits the Earth every 13.7 days on a highly elliptical orbit, scanning a sector of the sky spanning 24° × 96° for a total of two orbits, before moving on to the next sector. It captures images at 2-s (used for guiding), 20-s (for 1,000 bright asteroseismology targets), 120-s (for 200,000 stars that are probable planet hosts) and 30-min (full-frame image) cadences. The instrument consists of four CCD cameras, each with a field of view of 24° × 24°, with a wide band-pass filter from 600 to 1,000 nm (similar to the I_C band) and provides high-precision (approximately millimag) light curves for stars down to about 14 mag (I_C).

The NEOWISE mission uses a space-based infrared telescope that has been surveying the sky since 2013 at 3.4 and 4.6 μm. NEOWISE orbits near the Earth's day–night terminator, scanning rings of the sky near about 90° solar elongation and obtains a sequence of observations of a given region of sky every 6 months. The two wavelength channels are obtained simultaneously through a beam splitter, allowing for colour information to be extracted for each source detected in both bands. Detailed descriptions of NEOWISE operations and early results from the Reactivation mission[39] and the standard data processing and data characteristics[40] are available. A single data point for each epoch and wavelength is calculated by taking the weighted average of the individual NEOWISE measurements.

The ALMA data from programme 2019.A.00040.S were downloaded and processed through to a measurement set with CASA[41]. These observations were taken on 28 September 2021 (MJD = 59485) and used band 7, with a mean wavelength of 880 μm. No source is visible in the default archive products and we also detect no source at the expected location in CLEAN images. The archive products report an r.m.s. of 17 μJy and we measure an r.m.s. of 20 μJy in a naturally weighted image. We therefore consider these results as an upper limit of 60 μJy. In terms of the infrared excess visible in the mid-infrared with WISE, this upper limit is not at all constraining but does set limits on emission from cooler dust (Fig. 1).

Light curves

In this section, we consider the light curves; first, the implications of the TESS data for the stellar age and then the implications of the ground-based optical light curves for transverse velocity of the occulting material and dust grain sizes.

Stellar rotation and age. TESS data from the Quick-Look Pipeline[42,43] were retrieved from the Mikulski Archive for Space Telescopes (MAST) and are shown in Extended Data Fig. 2. The star was observed in sectors 8, 34 and 35. The star was observed soon after the infrared brightening and two sequential sectors some time later.

A periodic signal with a period of approximately 4.3 days is seen, with a peak-to-peak amplitude of 2% of the mean flux and the similar period can be seen in the two later sectors but they are overwhelmed with the first signs of debris from the transiting object. We carry out a Lomb–Scargle periodogram on S08 and obtain a notable detection of $P = 4.43 \pm 0.33$ days. A similar period is seen at lower significance in the later sectors. Apart from a peak at 1 day, the strongest peak in the ASAS-SN data has a similar period, at 4.1 days. We attribute this modulation to star spots on the star rotating in and out of our view, and so we assert that is the rotational period of the star. Using this rotational period, the gyrochronological age[44,45] is calculated to be 300 ± 92 Myr.

Duration of the eclipse and gradient analysis. Figure 2 shows the optical light curves. The start of the optical eclipse is seen around MJD 59350 in the g′ band observations and returns to pre-eclipse levels by MJD 59850, giving a total eclipse duration of approximately 500 days. The eclipse depth varies as a function of wavelength, which is discussed below. The normalization of the light curves for the ASAS-SN, ATLAS and ALLWISE photometry was performed by calculating the out-of-transit flux before MJD 58700. The LCOGT and AAVSO photometry was determined by aligning the photometry of the eclipse with the ASAS-SN and ATLAS photometry on a per-band basis. By treating the linear changes in flux as owing to the edges of large dust clouds crossing the disk of the star, and the largest amount of absorption in any of these segments as an estimate for the absorption of the cloud (see equations (4.2) and (4.3) in ref. 46), we can determine a robust lower limit to the transverse velocity of 7.5 km s^{-1} for the material moving in front of the star. The method is illustrated in Extended Data Fig. 3 and the results over the full optical transit are shown in Fig. 2b. We convert the magnitude $M(t)$ at time t to a normalized flux $f(t) = 10^{(M(t)-M_0/-2.5)}$, in which M_0 is the mean magnitude outside the eclipse. We visually determine turning points in the linearly increasing or decreasing photometric flux, fit straight lines to the selected points and determine the flux gradient in units of day^{-1}. A lower bound can be derived for the transverse velocity of the dust, v, by measuring the gradient of the light curve and determining what velocity a sharp-edged and completely opaque occulter moving across the disk of the star would need to make the same gradient. If the dust is on a circular orbit, it therefore has to be within 16 AU (equivalent to an orbital period of 63 years) around the star. The temperature of dust grains at this distance would be in the range 100–200 K.

Dust properties from optical colours. As is clear from Fig. 2, the photometry shows deeper absorption at bluer wavelengths compared with redder wavelengths. This wavelength-dependent absorption is typical of extinction because of particles with a characteristic size similar to or smaller than that of the observed wavelengths. The differences are quantified in Extended Data Fig. 4, which shows the AAVSO *BVI* photometric colours as a function of *V* magnitude. For both $B-V$ and $V-I$, the colour becomes redder as the star dims and the reddening is quantified here by the total to selective extinction ratio A_λ/A_V (dashed lines). The values are similar to those seen for interstellar extinction[47], indicating that the dimming is caused by submicrometre-sized dust[48,49]. A further constraint from the colours relates to scattering; in protoplanetary disk systems that undergo dimming (for example, UX Ori types), the colour initially reddens with dimming but moves back towards the stellar colour when the dimming is more than one or two magnitudes (for example, ref. 50). This 'blueing' is typically interpreted as the relative increase in dust-scattered starlight from the disk or envelope as the star itself fades[51]. This behaviour is also seen in Extended Data Fig. 4, in which $B-V$ shows marked blueing, whereas $V-I$ does not. The solid lines show an extinction model in which an underlying scattered-light component with the same colour as the star has been added; as the star dims, it reddens, but will eventually return to the stellar colour. This happens more quickly for $B-V$ because nearly all of the stellar flux in *B* is blocked and is less pronounced for $V-I$ because the star is substantially less dimmed in *I*. The fraction of scattered light is relatively large at 7.5%, implying an important complex of small dust around the star by the time the deepest parts of the optical transit occur. This high fraction suggests that the impact occurred a substantial fraction of an orbit before the optical transit, thus allowing the dust complex time to spread around the star.

Dust-mass estimates

The SED in Extended Data Fig. 1 gives an estimate of the infrared flux that would arise from dust thrown off in the putative collision. We assume that the collision occurred on the order of 10 AU from the star and hence that a dust temperature of 100 K is reasonable. Here 1% of the mass of a 20 $M_{\rm Earth}$ planet is assumed to be converted entirely into 0.1-μm-sized grains; this is an optimistic assumption given that the total mass thrown off in collisions is on the order 1% or less[52] and that this ejected mass is constituted of bodies of a range of sizes and all the mass is not present as dust. The dust spectrum in Extended Data Fig. 1 is approximated as a blackbody multiplied by $0.01 \times (10/\lambda)^{1.5}$ (with λ in μm), based on the absorption efficiency for silicates[53]. Changing the grain size to 1 μm yields a similar dust spectrum; although the dust-emitting area is less, these grains emit more efficiently. Thus, the mass in small grains detectable with ALMA is about 0.2 $M_{\rm Earth}$. The dust spectrum lies well below the WISE measurements and just below the ALMA measurement. Even in this optimistic case, thermal emission from dust thrown off in the collision is therefore not necessarily easily detected. This difference is one of surface area; at 600 pc, thousands of square AU of 100-K dust is needed for a thermal detection with ALMA, but only a small fraction of a square AU is needed to notably dim a star (which has radius of approximately 0.005 AU).

Alternative explanations for the observations

We consider three possible scenarios to explain the observations: (1) the initial brightening and later eclipse are two unrelated phenomena; (2) the infrared emission and optical transit are both produced by a debris disk at about 0.1 AU; (3) we are observing the aftermath of a collision between super-Earths or mini-Neptunes at a semimajor axis of several AU (see Extended Data Fig. 5). We provide here some more detail on the failures of the first two and a preliminary simulation illustrating how an impact between two large bodies can produce a large object as proposed for our preferred scenario.

First, the infrared flux increase and the optical dimming might be unrelated, coincidental phenomena. For example, one debris disk at 0.1 AU passively heated to 1,000 K producing the infrared emission and another disk further from the star that transited ASASSN-21qj. This explanation is unsatisfactory because both infrared flux increases and dimming events are rare. Mid-infrared excesses are exceptionally rare among main-sequence stars (1:10,000 (ref. 54)) and still uncommon for young stars (1:100 (ref. 54)), and no star has previously shown a sizeable increase starting from no excess. A single case of a disappearing mid-infrared excess has been seen, which remains largely unexplained[55]. Similarly, optical-dimming events are rare for main-sequence stars; for example, only one was seen to undergo dust-related optical dimming with the Kepler main mission, which observed 150,000 stars for 4 years (ref. 56). Both optical and infrared variability are independently less than 1% probabilities for a given star, so for ASASSN-21qj to show both by chance is at best a 0.01% probability, and probably much lower.

Another possibility is that both the infrared and optical features are produced by a single debris disk at about 0.1 AU from the star. At such a close distance, any dust clumps would initially produce periodic eclipses on the timescale of days[57] before being sheared into an azimuthally symmetric structure in months, so the occultation of the star would need to be related to changes in the vertical structure of a near-edge-on post-collision disk, for example, by dynamical 'stirring' of debris by impact remnants[58]. The optical depth of the disk must then decrease owing to continuing collisional depletion to explain the slow return to pre-transit levels of optical flux and gradual decrease in infrared flux. Three issues with this model are that: (1) the disk must have precisely the right geometry to slowly occult the star as the scale height increased and must coincidentally become optically thin; (2) there is no apparent change in dust temperature, which would be expected as the optical depth decreases and the warmer inner disk becomes visible; and (3) notable optical variation is seen 3 years after the putative collision, so any initially created clumps would already have sheared out. Newer clumps must contribute on the order of 50% of the dust area to explain the large variations around MJD 59500 but the infrared flux shows a gradual decline, rather than any strong variation that would be associated with clump creation. A fourth, but less critical, issue is that the inferred clump velocities are not as high as they could be for transiting structures at 0.1 AU, which should result in transverse velocities of up to 100 km s^{-1}.

Smoothed particle hydrodynamics collision simulations

To provide some more insight into the collision scenario, we performed impact simulations using the SWIFT smoothed particle hydrodynamics (SPH) code[59–61]. Extended Data Fig. 6 shows a collision between two 25 $M_{\rm Earth}$ planets at 45.77 km s^{-1} (1.4 $v_{\rm esc}$, escape velocity neglecting the atmosphere) at an impact parameter of 0.4 (an impact angle of 23.6°). The colliding bodies were 22.5% rock (forsterite)[62,63], 67.5% water[64] and 10% H/He (ref. 65) by mass. 2.1×10^6 particles were used in the simulation. To make simulations with high resolution numerically tractable, SWIFT imposes a maximum smoothing length that, in effect, imposes a minimum density for particles in the simulation (about 30 kg m^{-3} for the simulation shown here). The bound post-impact material is spread over hundreds of Earth radii following the collision, illustrating that giant impacts can produce very large post-impact objects.

However, for the massive and highly extended bodies produced by collisions between super-Earths and mini-Neptunes, a large fraction of the post-impact body is at the minimum density (green particles in lower-right panel in Extended Data Fig. 6). SPH simulations therefore probably underestimate the extent of such post-impact bodies and further work is needed to fully quantify the size of post-impact bodies produced in different impacts.

Post-impact body-cooling calculations

How the emission from a post-impact body would evolve with time is highly dependent on the initial mass distribution and thermal state of the body, and the balance between radiative cooling, viscous spreading and mass and angular momentum transport by condensates[12,20,29]. Given the limitations of SPH simulations (see above), it is not possible to accurately determine the initial structure of post-impact bodies in the relevant regime. To explore a range of possible evolution pathways, we have calculated the evolution of post-impact bodies with different power-law surface-density profiles, Σ, under the limiting case that radiative cooling and condensation of the vapour is the single driver for evolution of the structure. We chose a power-law surface-density profile as it can straightforwardly cover the wide range of surface-density profiles expected after super-Earth/mini-Neptune collisions, based on those found in impact simulations between lower-mass, terrestrial bodies[12,19,66–69]. The surface-density profile is given by:

$$\Sigma = \begin{cases} \Sigma_0, & \text{if } r_{xy} \le R_{\rm c} \\ \alpha r_{xy}^{\beta}, & \text{if } R_{\rm c} < r_{xy} \le R_{\rm emit} \\ 0, & \text{if } r_{xy} > R_{\rm emit} \end{cases} \quad (1)$$

in which r_{xy} is the distance from the rotation axis; $R_{\rm c}$ is the outer radius of a constant-surface-density central region, roughly analogous to the corotating regions seen in Earth-mass synestias[12,20]; Σ_0 is the surface density of the central region; β is the power-law exponent; and $R_{\rm emit}$ is the initial emitting radius. Imposing surface-density continuity gives:

$$\alpha = \Sigma_0 R_{\rm c}^{-\beta}. \quad (2)$$

We can determine Σ_0 by fixing the mass of the body

$$M_{\rm p} = \int_0^{R_{\rm c}} 2\pi r'_{xy}\, \Sigma_0 {\rm d}r'_{xy} + \int_{R_{\rm c}}^{R_{\rm emit}} 2\pi r'_{xy}\, \Sigma(r'_{xy}) {\rm d}r'_{xy}, \quad (3)$$

which can be solved to give:

$$\Sigma_0 = \begin{cases} \dfrac{M_{\rm p}}{\pi[R_{\rm c}^2 + 2R_{\rm c}^{-\beta}(\ln R_{\rm emit} - \ln R_{\rm c})]}, & \text{if } \beta = -2, \\ \dfrac{M_{\rm p}}{\pi\left[R_{\rm c}^2 + \frac{2R_{\rm c}^{-\beta}}{\beta+2}(R_{\rm emit}^{\beta+2} - R_{\rm c}^{\beta+2})\right]}, & \text{otherwise.} \end{cases} \quad (4)$$

The time taken for a given region of the structure to cool to the point that a sufficient fraction of material is condensed for the temperature to drop below the condensation buffer (see above)—and thus for the emitted flux to drop—is given by

$$t_{\rm cool}(r_{xy}) = \frac{lf(r_{xy})\Sigma(r_{xy})}{\sigma T_{\rm emit}^4} \quad (5)$$

in which f is the initial vapour fraction at that radius, l is the latent heat of vaporization of the material (here we have taken the limiting case of pure water $l = 2.256 \times 10^6$ (ref. 70), but the addition of silicates could make the latent heat much larger), σ is the Stefan–Boltzmann constant

and T_{emit} is the emission temperature. Figure 3 shows example evolutions of the emission from a post-impact body using this model for different parameters (solid lines). Results of a modified model in which the initial surface density (by the addition of a constant parameter to equation (1)) is forced to be zero at R_{emit} are shown as dashed lines.

Data availability

The datasets generated and analysed during this study are available in the Zenodo repository at https://doi.org/10.5281/zenodo.8344755.

Code availability

All the code for the analysis and the generation of all the figures are available in a showyourwork[71] reproducible framework available as a git repository at https://github.com/mkenworthy/ASASSN-21qj-collision/. The source code and documentation for the SWIFT open-source simulation code are available from www.swiftsim.com.

30. Yelverton, B., Kennedy, G. M., Su, K. Y. L. & Wyatt, M. C. A statistically significant lack of debris discs in medium separation binary systems. *Mon. Not. R. Astron. Soc.* **488**, 3588–3606 (2019).
31. Booth, M. et al. Resolved debris discs around A stars in the Herschel DEBRIS survey. *Mon. Not. R. Astron. Soc.* **428**, 1263–1280 (2013).
32. Pawellek, N. & Krivov, A. V. The dust grain size–stellar luminosity trend in debris discs. *Mon. Not. R. Astron. Soc.* **454**, 3207–3221 (2015).
33. Pojmanski, G. The All Sky Automated Survey. *Acta Astron.* **47**, 467–481 (1997).
34. Pojmanski, G. All Sky Automated Survey Catalog. VizieR On-line Data Catalog: J/other/AcA/50. *CDS* https://cdsarc.cds.unistra.fr/viz-bin/cat/J/AcA/50/177 (2005).
35. Simon, J. D. et al. KIC 8462852 ASAS V-band long-term variability. VizieR On-line Data Catalog: J/ApJ/853/77. *CDS* https://cdsarc.cds.unistra.fr/viz-bin/cat/J/ApJ/853/77 (2018).
36. Hambsch, F.-J. ROAD (Remote Observatory Atacama Desert): intensive observations of variable stars. *J. Am. Assoc. Variable Star Observers* **40**, 1003–1009 (2012).
37. Tonry, J. L. et al. ATLAS: a high-cadence all-sky survey system. *Proc. Astron. Soc. Pac.* **130**, 064505 (2018).
38. Ricker, G. R. et al. Transiting Exoplanet Survey Satellite (TESS). *J. Astron. Telesc. Instrum. Syst.* **1**, 014003 (2015).
39. Mainzer, A. et al. Initial performance of the NEOWISE reactivation mission. *Astrophys. J.* **792**, 30 (2014).
40. Cutri, R. M. et al. *Explanatory Supplement to the NEOWISE Data Release Products* (Infrared Processing and Analysis Center, 2015); https://wise2.ipac.caltech.edu/docs/release/neowise/expsup/.
41. McMullin, J. P., Waters, B., Schiebel, D., Young, W. & Golap, K. CASA architecture and applications. In *Proc. Astronomical Data Analysis Software and Systems XVI, ASP Conference Series* Vol. 376 (eds Shaw, R. A. et al.) 127–130 (Astronomical Society of the Pacific, 2007).
42. Huang, C. X. et al. Photometry of 10 million stars from the first two years of TESS full frame images: part I. *Res. Notes AAS* **4**, 204 (2020).
43. Kunimoto, M. et al. Quick-look pipeline lightcurves for 9.1 million stars observed over the first year of the TESS Extended Mission. *Res. Notes AAS* **5**, 234 (2021).
44. Bouma, L. G., Palumbo, E. K. & Hillenbrand, L. A. The empirical limits of gyrochronology. *Astrophys. J. Lett.* **947**, L3 (2023).
45. Kounkel, M. et al. Untangling the galaxy. IV. Empirical constraints on angular momentum evolution and gyrochronology for young stars in the field. *Astron. J.* **164**, 137 (2022).
46. Kennedy, G. M. et al. The transiting dust clumps in the evolved disc of the Sun-like UXor RZ Psc. *R. Soc. Open Science* **4**, 160652 (2017).
47. Cardelli, J. A., Clayton, G. C. & Mathis, J. S. The relationship between infrared, optical, and ultraviolet extinction. *Astrophys. J.* **345**, 245–256 (1989).
48. Mathis, J. S., Rumpl, W. & Nordsieck, K. H. The size distribution of interstellar grains. *Astrophys. J.* **217**, 425–433 (1977).
49. Weingartner, J. C. & Draine, B. T. Dust grain-size distributions and extinction in the Milky Way, Large Magellanic Cloud, and Small Magellanic Cloud. *Astrophys. J.* **548**, 296–309 (2001).
50. Herbst, W., Herbst, D. K., Grossman, E. J. & Weinstein, D. Catalogue of UBVRI photometry of T Tauri stars and analysis of the causes of their variability. *Astron. J.* **108**, 1906–1923 (1994).
51. Grinin, V. P. On the blue emission visible during deep minima of young irregular variables. *Sov. Astron. Lett.* **14**, 27 (1988).
52. Leinhardt, Z. M. & Stewart, S. T. Collisions between gravity-dominated bodies. I. Outcome regimes and scaling laws. *Astrophys. J.* **745**, 79 (2012).
53. Laor, A. & Draine, B. T. Spectroscopic constraints on the properties of dust in active galactic nuclei. *Astrophys. J.* **402**, 441 (1993).
54. Kennedy, G. M. & Wyatt, M. C. The bright end of the exo-Zodi luminosity function: disc evolution and implications for exo-Earth detectability. *Mon. Not. R. Astron. Soc.* **433**, 2334–2356 (2013).
55. Melis, C. et al. Rapid disappearance of a warm, dusty circumstellar disk. *Nature* **487**, 74–76 (2012).
56. Boyajian, T. S. et al. Planet Hunters IX. KIC 8462852—where's the flux? *Mon. Not. R. Astron. Soc.* **457**, 3988–4004 (2016).
57. Gaidos, E. et al. Planetesimals around stars with TESS (PAST)—I. Transient dimming of a binary solar analogue at the end of the planet accretion era. *Mon. Not. R. Astron. Soc.* **488**, 4465–4476 (2019).
58. Ida, S. & Makino, J. *N*-body simulation of gravitational interaction between planetesimals and a protoplanet: I. velocity distribution of planetesimals. *Icarus* **96**, 107–120 (1992).
59. Schaller, M., Gonnet, P., Chalk, A. B. G. & Draper, P. W. SWIFT: using task-based parallelism, fully asynchronous communication, and graph partition-based domain decomposition for strong scaling on more than 100,000 cores. In *Proc. Platform for Advanced Scientific Computing Conference* 1–10 (ACM, 2016).
60. Schaller, M. et al. SWIFT: SPH with inter-dependent fine-grained tasking. *Astrophysics Source Code Library* ascl:1805.020 (2018).
61. Kegerreis, J. A. et al. Planetary giant impacts: convergence of high-resolution simulations using efficient spherical initial conditions and SWIFT. *Mon. Not. R. Astron. Soc.* **487**, 5029–5040 (2019).
62. Stewart, S. T. et al. Equation of state model forsterite-ANEOS-SLVTv1.0G1: documentation and comparisons. *Zenodo* https://doi.org/10.5281/zenodo.3478631 (2019).
63. Stewart, S. et al. The shock physics of giant impacts: key requirements for the equations of state. *AIP Conf. Proc.* **2272**, 080003 (2020).
64. Senft, L. E. & Stewart, S. T. Impact crater formation in icy layered terrains on Mars. *Meteorit. Planet. Sci.* **43**, 1993–2013 (2008).
65. Hubbard, W. B. & MacFarlane, J. J. Structure and evolution of Uranus and Neptune. *J. Geophys. Res. Solid Earth* **85**, 225–234 (1980).
66. Canup, R. M. Forming a Moon with an Earth-like composition via a giant impact. *Science* **338**, 1052–1055 (2012).
67. Ćuk, M. & Stewart, S. T. Making the Moon from a fast-spinning Earth: a giant impact followed by resonant despinning. *Science* **338**, 1047–1052 (2012).
68. Rufu, R., Aharonson, O. & Perets, H. B. A multiple-impact origin for the Moon. *Nat. Geosci.* **10**, 89–94 (2017).
69. Reufer, A., Meier, M. M., Benz, W. & Wieler, R. A hit-and-run giant impact scenario. *Icarus* **221**, 296–299 (2012).
70. Chase, M. W. Jr *NIST-JANAF Thermochemical Tables* 4th edn (American Chemical Society and the American Institute of Physics for the National Institute of Standards and Technology, 1998).
71. Luger, R. et al. Mapping stellar surfaces III: an efficient, scalable, and open-source Doppler imaging model. Preprint at https://arxiv.org/abs/2110.06271 (2021).
72. Gaia Collaboration et al. Gaia Data Release 3. Summary of the content and survey properties. *Astron. Astrophys.* **674**, A1 (2023).
73. Bailer-Jones, C. A. L., Rybizki, J., Fouesneau, M., Demleitner, M. & Andrae, R. Estimating distances from parallaxes. V. Geometric and photogeometric distances to 1.47 billion stars in Gaia Early Data Release 3. *Astron. J.* **161**, 147 (2021).
74. Cutri, R. M. et al. 2MASS All-Sky Catalog of Point Sources. VizieR On-line Data Catalog: II/246. *CDS* https://cdsarc.cds.unistra.fr/viz-bin/cat/II/246 (2003).
75. Henden, A. A., Levine, S., Terrell, D. & Welch, D. L. APASS—the latest data release. *Am. Astron. Soc. Meeting Abstr.* **225**, 336.16 (2015).
76. Pecaut, M. J. & Mamajek, E. E. Intrinsic colors, temperatures, and bolometric corrections of pre-main-sequence stars. *Astrophys. J. Suppl. Ser.* **208**, 9 (2013).

Acknowledgements G.K. is supported by the Royal Society as a Royal Society University Research Fellow. S.J.L. acknowledges funding from the UK Natural Environment Research Council (grant NE/V014129/1). L.C. acknowledges funding from the European Union H2020-MSCA-ITN-2019 under grant agreement no. 860470 (CHAMELEON). J.D. acknowledges funding support from the Chinese Scholarship Council (no. 202008610218). Giant impact simulations were carried out using the Isambard 2 UK National Tier-2 HPC Service (http://gw4.ac.uk/isambard/) operated by GW4 and the UK Met Office and funded by EPSRC (EP/T022078/1). We thank K. Stanek and the work of the ASAS-SN team with their survey and for providing public access to the database. Part of this research was carried out at the Jet Propulsion Laboratory, California Institute of Technology, under a contract with the National Aeronautics and Space Administration (80NM0018D0004).

Author contributions M.K. led the writing of the paper, management, obtaining the optical observations and initial models. S.L. led the afterglow modelling and theory. G.K. led the orbital analysis and dust analysis. R.v.C. carried out the optical-light-curve-data reduction and reddening analysis and velocity-constraint analysis. E.M. performed the analysis of the properties of the star. F.-J.H. and E.G. carried out optical monitoring of the star. J.M., A.M., J.D.K. and A.S. were responsible for NEOWISE identification and data reduction. S.L., L.C., J.D., P.T. and Z.L. provided discussion on the ejected material and subsequent evolution. J.D. performed the SPH impact simulations. H.B., S.C., O.G., P.L.D., L.M. and P.T. were responsible for the observation and reduction of observational data. M.R.S. led the discovery of the optical dimming of the star. All co-authors assisted with manuscript writing and proofreading.

Competing interests The authors declare no competing interests.

Additional information

Correspondence and requests for materials should be addressed to Matthew Kenworthy.

Peer review information *Nature* thanks Kate Su and the other, anonymous, reviewer(s) for their contribution to the peer review of this work.

Reprints and permissions information is available at http://www.nature.com/reprints.

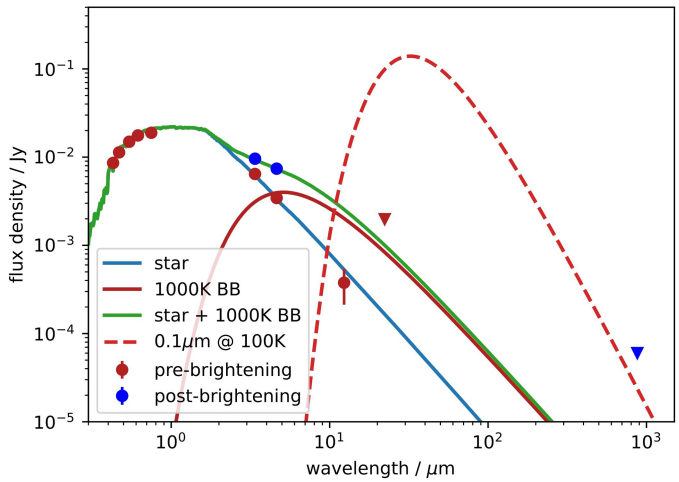

Extended Data Fig. 1 | Spectrum of ASASSN-21qj components. The red symbols show the optical and pre-brightening WISE infrared photometry and the blue symbols show the post-brightening WISE and ALMA fluxes. Stellar and 1,000 K components consistent with the pre-brightening and post-brightening fluxes are shown. The dashed line shows an estimated cool-component spectrum for 0.1-μm-sized grains associated with the transiting dust cloud. Downward triangles are upper limits. Error bars are shown at 1σ confidence.

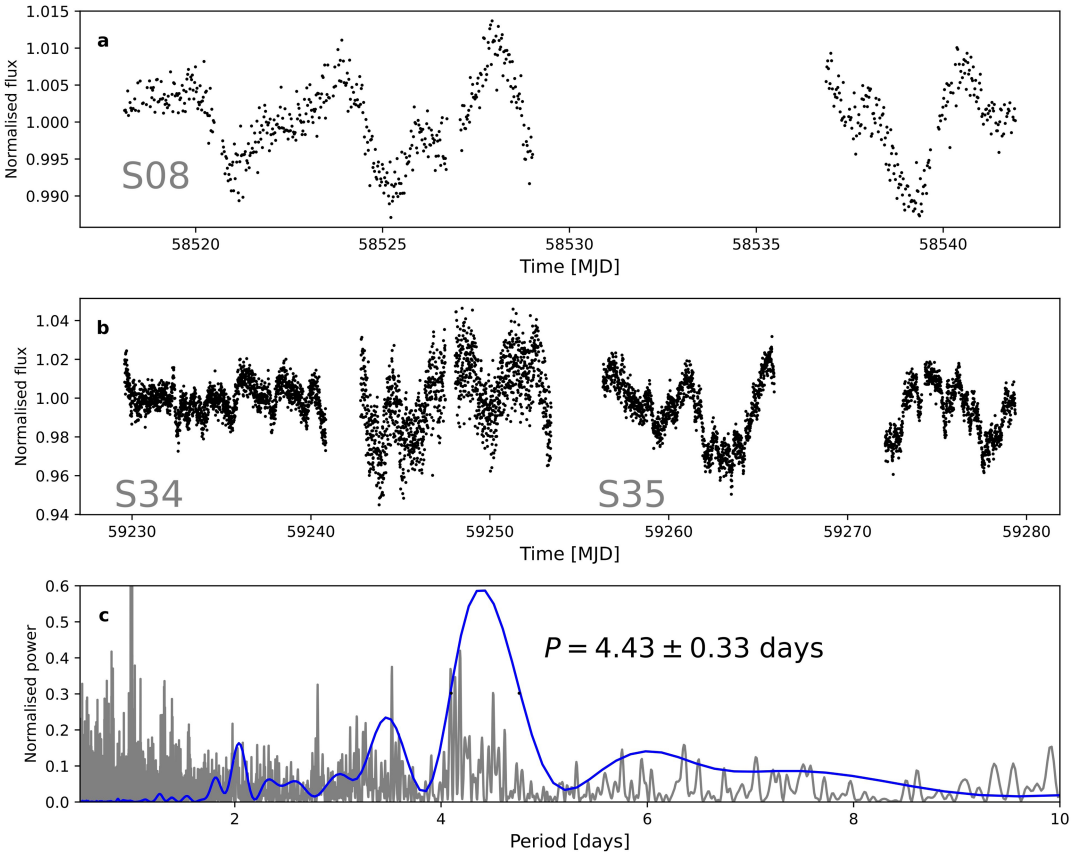

Extended Data Fig. 2 | The light curve of ASASSN-21qj from TESS and the periodogram of TESS and ASAS-SN photometry. a,**b**, Photometry of ASASSN-21qj from three sectors of TESS. **c**, Lomb–Scargle analysis of photometry from TESS (coloured blue) and from ASAS-SN V-band data from MJD 57420 to MJD 58386 (light grey) shows a signal at 4.4 days. At lower frequencies, the ground-based photometry shows power and aliasing signals. The TESS signal shows an important signal at 4.43 days, and a similar signal is seen in the ground-based data. The longer time baseline in the ASAS-SN data reveals substructure in the signal.

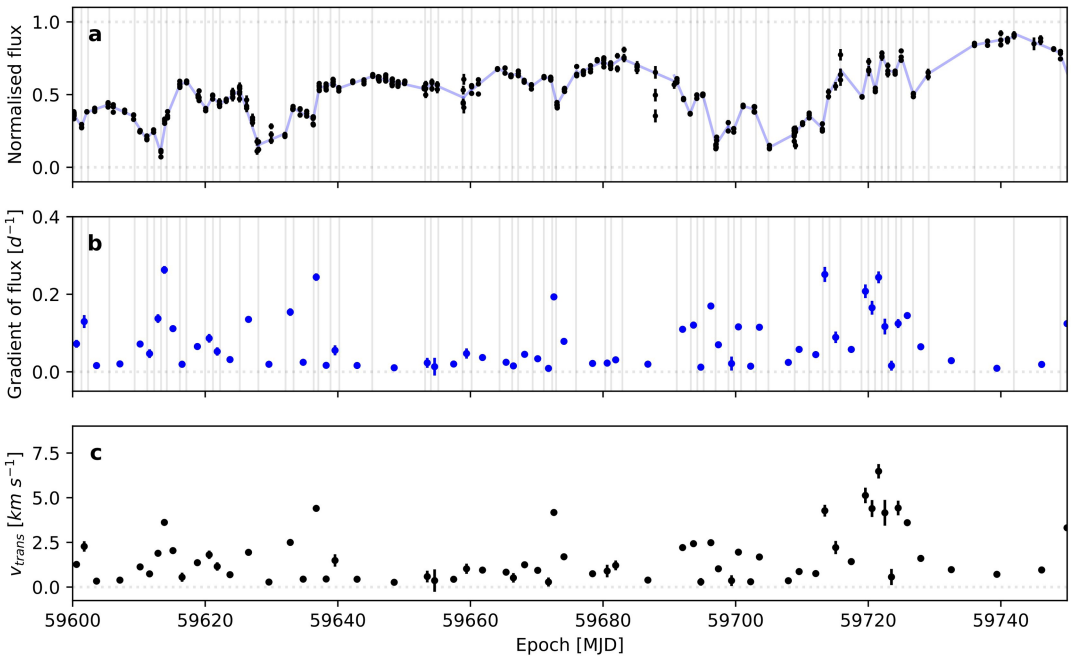

Extended Data Fig. 3 | Deriving the transverse velocity from a light curve. **a**, ASAS-SN g′ photometry is shown in units of normalized flux. Straight-line fits (light-blue lines) are made to the photometry in the regions indicated by the light-grey vertical lines. **b**, Gradient of the light curve as a function of time. **c**, Transverse velocity derived from the light curve and the gradient of the light curve. Error bars are shown at 1σ confidence.

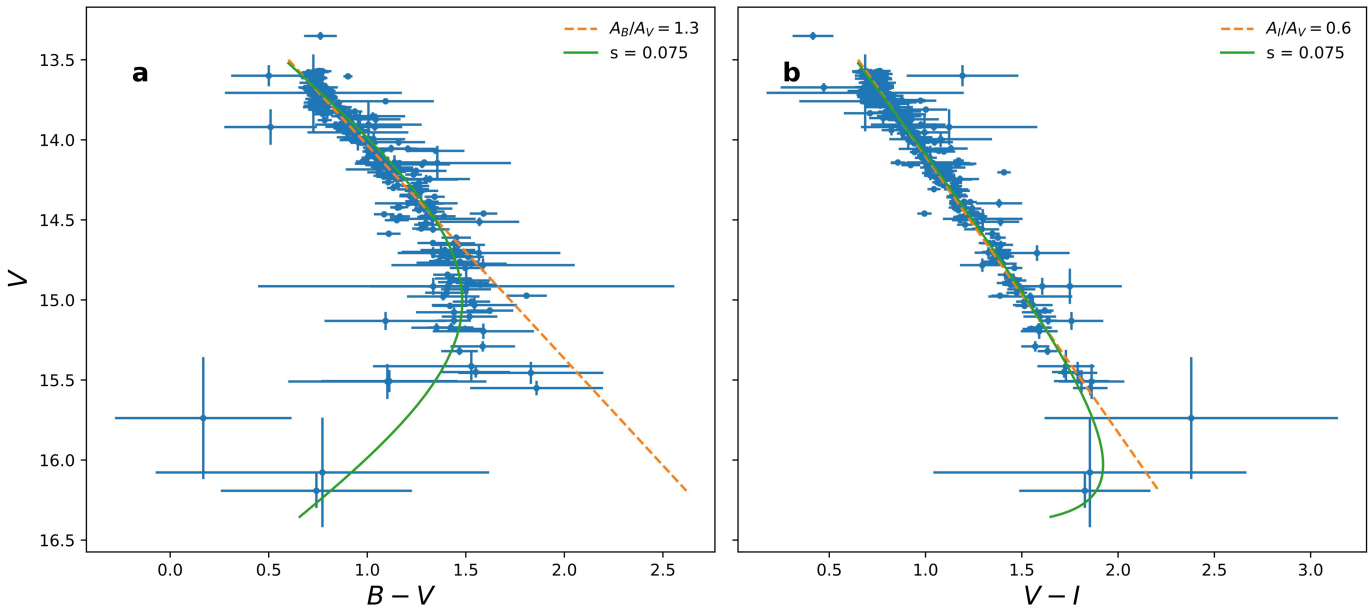

Extended Data Fig. 4 | Blueing of the *B*–*V* and *V*-*I* colours during the dimming event. Points show AAVSO data and lines show models. **a**, The *V* magnitude versus *V*-*I* colour and **b**, the *V* magnitude versus *V*-*I* colour. The dashed line is a line of A_λ/A_V for the value shown in the legend and the solid line is a model that includes an underlying scattered-light component with $s = 7.5\%$ of the stellar flux. Error bars are shown at 1σ confidence.

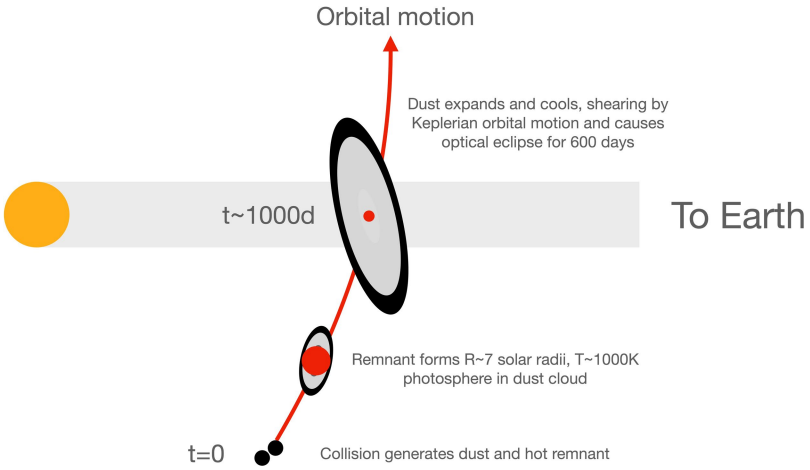

Extended Data Fig. 5 | Sketch of the hypothesis for the observations seen towards ASASSN-21qj. At $t = 0$, the collision occurs, producing a cloud of debris that expands and cools. Material close to the remnant is heated by its luminosity, generating the 1,000 K infrared emission. Around 1,000 days later, the expanding cloud crosses the line of sight between the star and the Earth, generating the optical light curve.

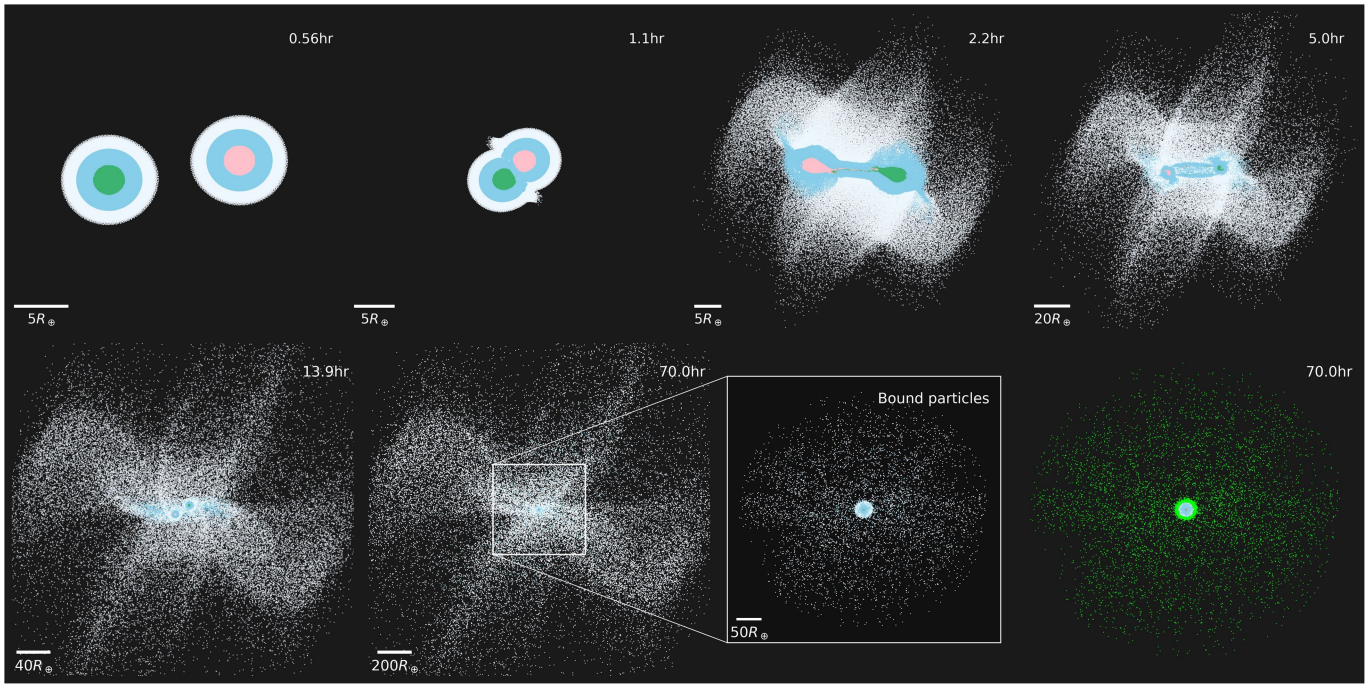

Extended Data Fig. 6 | Simulations of the formation of a post-impact body. Giant impacts between super-Earths and mini-Neptunes can produce post-impact bodies hundreds of Earth radii across, comparable with that required to produce the observed infrared flux. With the exception of the lower-right panel, particles are coloured by their material (forsterite, water or a H_2–He mixture moving outwards in the initial bodies) and whether they came from the impactor or target (see top-left panel). The final two panels show just the mass bound to the primary remnant, which has a mass of 48.4 M_{Earth}. In the final panel, particles that are at the minimum density imposed by the code are coloured in green.

Extended Data Table 1 | Properties of ASASSN-21qj

Property	Value
α_{ICRS}, [hh mm ss]	08:15:23.30[1]
δ_{ICRS}, [dd mm ss]	-38:59:23.3[1]
μ_α [mas yr^{-1}]	-9.692 ± 0.012[1]
μ_δ [mas yr^{-1}]	7.349 ± 0.012[1]
ϖ [mas]	1.763 ± 0.011[1]
RV [km s^{-1}]	25.8 ± 3[1]
Distance [pc]	$567.2^{+6.7}_{-5.9}$[2]
G [mag]	13.371 ± 0.003[1]
G_{BP} [mag]	13.697 ± 0.003[1]
G_{RP} [mag]	12.882 ± 0.004[1]
$G_{BP} - G_{RP}$ [mag]	0.815 ± 0.005[1]
J [mag]	> 12.07[3]
H [mag]	12.03 ± 0.04[3]
K_s [mag]	11.99 ± 0.04[3]
B (AB) [mag]	14.16 ± 0.06[4]
V (AB) [mag]	13.48 ± 0.03[4]
g' (AB) [mag]	13.77 ± 0.03[4]
r' (AB) [mag]	13.29 ± 0.03[4]
i' (AB) [mag]	13.20 ± 0.08[4]
$T_{\rm eff}$ [K]	5760 ± 10[1]
[Fe/H] [dex]	-0.23 ± 0.01[1]
$\log g$ [$\log_{10}$ cm s^{-2}]	4.339 ± 0.005[1]
R_* [$R_\odot$]	1.04[5]
$\log(L_{bol}/L_\odot)$ [dex]	0.033[5]
m_{bol} [mag]	13.49 ± 0.02[6]
$E(G_{BP} - G_{RP})$ [mag]	0.01 ± 0.005[6]
Age [Myr]	300 ± 92[7]

[1]Gaia DR3 (ref. 72), coordinates are J2000 at epoch 2000.0. [2]Reference 73. [3]2MASS[74], *J* is an upper limit and *H* and K_s are flagged as contaminated. [4]APASS[75], this photometry includes a nearby star. [5]Estimated from an SED fit fixed to Gaia properties. [6]Estimated using mean stellar properties[76]. [7]Estimated using rotation period.

Extended Data Table 2 | Photometric observations of ASASSN-21qj

Survey name	Filter	Number of points
ASASSN	V	758
	g'	3225
ATLAS	c	161
	o	677
AAVSO	B	729
	I	728
	V	722
LCOGT	g	275
	r	224
	i	168
NEOWISE	$W1$	18
	$W2$	18

The number of points are listed per survey and filter. This is the count after initial rejection of photometric points with notably large error bars. Further photometric points may have been rejected in the different analysis steps. The ROAD observations constitute most of the observations from the AAVSO datasets.